Band Formation in a New England Winter Storm

DAWN G. WOLFSBERG,* KERRY A. EMANUEL AND RICHARD E. PASSARELLI†

Center for Meteorology and Physical Oceanography, Massachusetts Institute of Technology, Cambridge, MA 02139

(Manuscript received 17 December 1984, in final form 10 February 1986)

ABSTRACT

This case study addresses mechanisms of band formation in a New England winter storm. The structure of the bands and their environment are documented with synoptic observations, radar data, and analyses of instrumented aircraft flights through the bands. We postulate that processes on three scales are responsible for the bands observed, that the bands are probably a manifestation of mesoscale symmetric instability, and that potential energy for the instability is generated by synoptic scale differential lapse rate advection and converted to kinetic energy by symmetric overturning. Frontogenetical forcing results in an intermediate or subsynoptic scale region of ascent which brings the atmosphere to saturation and initiates the release of potential energy.

1. Introduction

On 11 December 1982, all of the precipitation in central New England due to a cyclonic storm fell from weak, but well-organized bands which were aligned along the thermal wind. This storm was observed as part of the New England Winter Storm Experiment, one purpose of which was to explore the hypothesis that conditional symmetric instability (CSI), also referred to as moist slantwise convection, may be responsible for many of the bands found in northeastern storms. The observations of strong vertical wind shear and low static stability suggest CSI as a feasible mechanism for band formation. However, the slantwise convection appears to have been enhanced by a subsynoptic scale region of frontogenetical activity in which the bands were embedded. Other studies (Emanuel, 1983b) have found that bands tend to exist in an environment which is nearly neutral to slantwise convection. This observation has been interpreted to indicate that the atmosphere is adjusted from a symmetrically unstable to neutral state as the instability is released. In this case, the conditions of instability appear to last longer than any of the individual bands. This observation leads us to investigate the sources and sinks of energy for CSI in the storm.

The quasi-two-dimensional bands frequently found in extra-tropical cyclones have attracted a great deal of attention. Linear organization of precipitation structures was noted by Austin (1960) in one of the first studies with weather radar. Houze et al. (1976) and Hobbs (1978) present comprehensive analyses of bands observed in cyclonic storms in the Pacific Northwest. They note that bands can occur in every sector of the storm. Elliot and Hovind (1964) observe a large number of bands in California and note that the axes of the bands tend to lie along the mean vertical shear vector.

A number of mechanisms for band formation have been proposed. Harrold (1973) suggested that frontal circulations carry buoyant air to regions of band growth. Other possibilities include ducted gravity waves (Lindzen and Tung, 1976), density currents (Carbone, 1982), and symmetric instability (Emanuel, 1979; Bennetts and Hoskins, 1979).

Some of these mechanisms can be ruled out in the present case. Harrold's "conveyor belt" model is not a candidate because there was no conditional instability. Although the temperature structure of the atmosphere may have allowed ducted gravity waves during the storm, evidence in the form of strong small-scale pressure fluctuations was not found in microbarograph traces or in hourly pressure reports.

In section 2, we describe the data set and the experiment. The bands and their environment are characterized in section 3. In section 4, we explore the role of symmetric instability. We first review a simple model of the instability and use the results to show that the environment was susceptible to CSI during the storm. Then we develop an expression for the time rate of change of available energy for CSI. Rough estimates of the terms in this expression suggest that the supply of potential energy was maintained by large-scale geostrophic lapse rate advection. In section 5, we provide discussion and conclusions.

2. Data and experimental design

Field observations for the case study include Doppler radar data, instrumented aircraft measurements, upper

* Present affiliation: School of Meteorology, University of Oklahoma, Norman, OK.

† Present affiliation: Sigmet, Inc., Acton, MA.

air data and surface observations. These are described below.

There are continuous observations from MIT's 11.03 cm radar for the duration of the storm. Constant-altitude-plan-position indicator (CAPPI) and range-height indicator (RHI) displays are analyzed for band structure.

At 1230 GMT and at 1830 GMT, the NCAR Queen Air instrumented airplane flew a series of four passes centered on a snowband at pressure levels 910, 815, 725 and 645 mb. Each pass was approximately 50 km long and was centered on the band observed with MIT radar. The airplane instruments recorded temperature, velocity, humidity, and cloud physical parameters every second. The data were averaged over 10 sec, or about 1 km air distance before analysis.

During the last half of the 1830 GMT flight, the band showed significant movement in the band-normal direction. The data were transformed into a band-relative coordinate system, oriented and moving with the band. Data points on the 725 and 645 mb passes were respectively shifted 10 and 20 km in the positive band-normal direction because the band had moved these distances at the time the data were taken. The band-relative, cross-band wind velocity in those two passes was calculated by subtracting the band-normal velocity of the band, 4 m s^{-1}, from the observed cross-band wind velocity.

The National Meteorological Center's standard upper air and surface data were supplemented by special radiosonde launches at 12 GMT and 18 GMT at MIT and at 18 GMT at Chatham, Massachusetts, and Albany, New York.

Fig. 1 shows the sites mentioned in this paper and the upper air network in the Northeast. The location of a vertical cross section is also indicated.

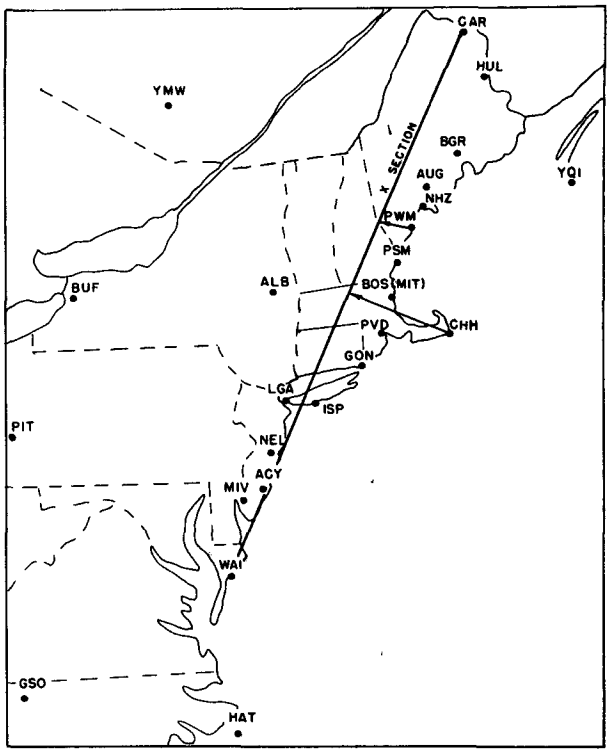

FIG. 1. Locations mentioned in the text. Stations are shown by three-letter code. A vertical cross section is indicated by the solid line.

3. Description of bands and their environment

a. The large-scale environment

The synoptic-scale weather pattern in New England on 11 December 1982 is dominated by a deep cyclone centered on Hudson Bay. Figure 2 shows geopotential heights, wind, and temperatures at 00 and 12 GMT. The vertical shear over central New England at 850 mb was directed toward 70°. The magnitude of the vertical shear in the vicinity of the bands was fairly high. The vertical shear at Chatham was greater than or equal to 7.5 m s^{-1} km^{-1} between 850 and 700 mb at 00 GMT, between 650 and 550 mb at 1200 GMT and between 625 and 525 mb at 18 GMT. The geostrophic shear backs with height, as can be inferred from the isotherms in Fig. 2. For example, at 00 GMT, the thermal wind is more southerly at 500 mb than at 850 mb.

The center of the storm and presumably the bulk of the upward motion are to the south and west of New England. Of the six maps in Fig. 2, only the 00 GMT, 850 mb chart shows significant geostrophic warm advection.

Figure 2 shows significant ageostrophy over New England. At 00 GMT, the velocity magnitudes at 850 and 700 mb are typically 80% of their geostrophic values. At 12 GMT, the 850 mb chart (Fig. 2d) shows substantial ageostrophic warm advection at Chatham, Massachusetts, and ageostrophic cold advection at Portland, Maine, and Albany, New York.

The 00 and 12 GMT sea level pressure maps in Fig. 3 indicate the presence of surface fronts. A cold front west of Wisconsin at 00 GMT advances eastward at about 8 m s^{-1}. It is ascertained from vertical cross sections oriented east to west (not shown) that there is very little east–west slope of potential isotherms over New England before about 18 GMT. The cold front probably does not affect the bands in New England until quite late in the case period. The frontogenesis evidenced by the warm front just south of Massachusetts is discussed below.

The thermal structure of the atmosphere over New England is illustrated in Fig. 4, which shows the Chatham sounding at 00 GMT. Features of the sounding include a frontal layer near 800 mb, an almost moist adiabatic temperature profile through the mid-troposphere, extensive moisture, and strong vertical wind shear. These characteristics are observed on most soundings from the Northeast on 11 December 1982.

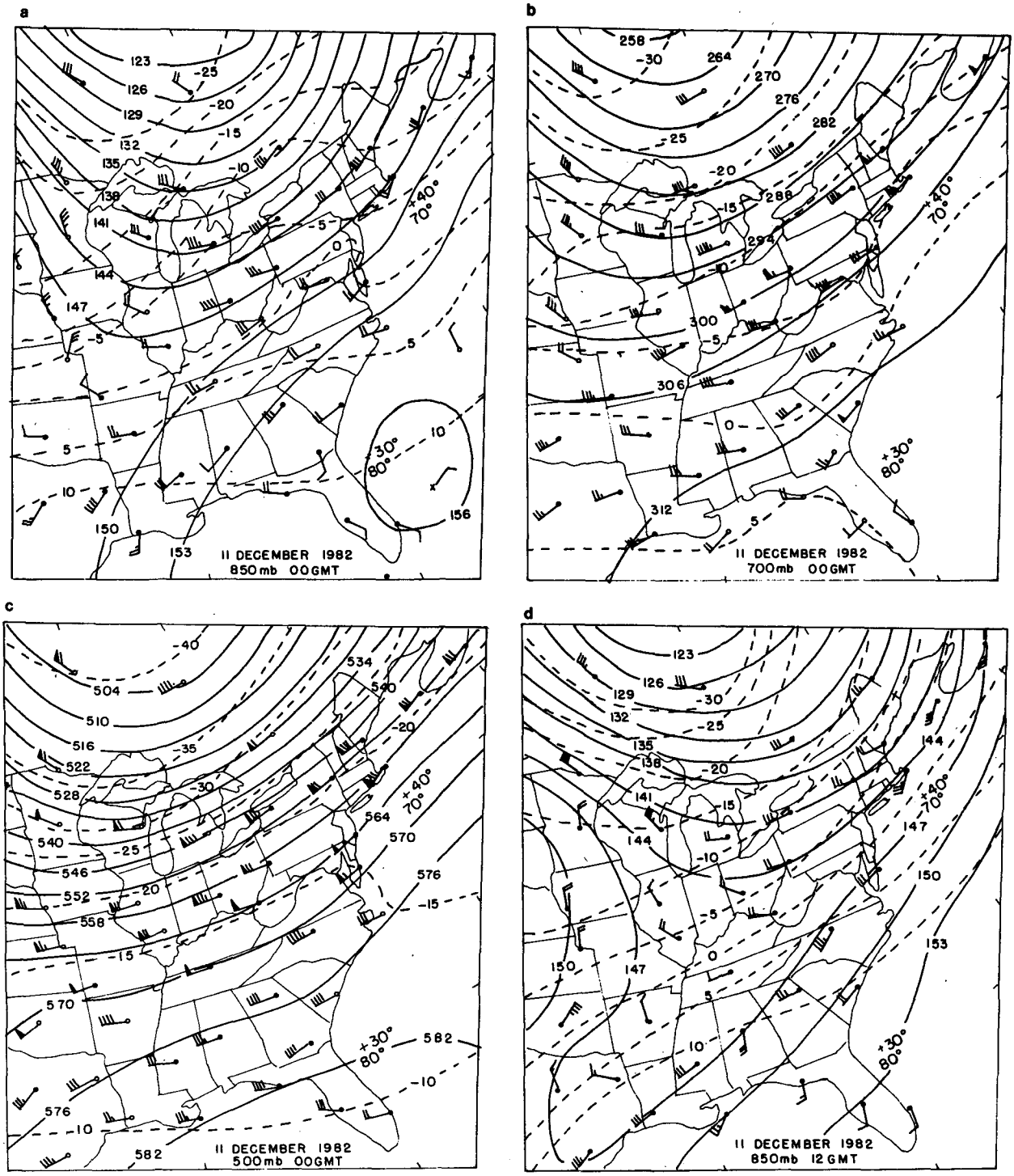

FIG. 2. Upper air charts on 11 December 1982 for (a) 850 mb at 00 GMT, (b) 700 mb at 00 GMT, (c) 500 mb at 00 GMT, (d) 850 mb at 12 GMT, (e) 700 mb at 12 GMT, and (f) 500 mb at 12 GMT. Solid lines are geopotential heights in dm and dashed lines are isotherms in °C. Winds are indicated with barbed velocity vectors (½ barb = 5 kt, 1 barb = 10 kt, triangular barb = 50 kt).

b. Frontogenetical forcing

The presence of a strong warm front in Fig. 3 suggests that frontogenetical forcing may be an environmental factor conducive to band formation in this case. Other researchers have noted cases in which both frontogenesis and symmetric instability are active. Sanders and Bosart (1985) found evidence for both in the "megalo-

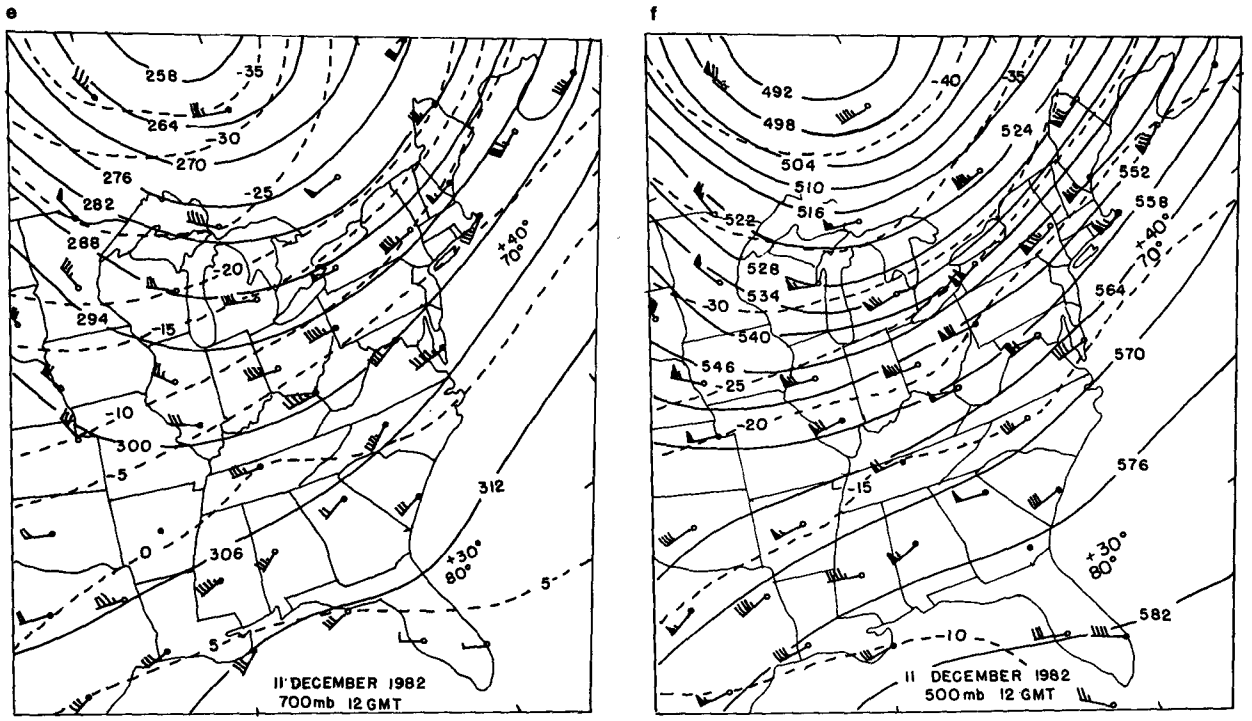

FIG. 2. (*Continued*)

politan snowstorm" of 11–12 February 1983. Gyakum (personal communication, 1985) has analyzed a large snowband in Illinois associated with the same system studied here, but which occurred approximately 24 hours prior to the case period we consider. He believes that although the atmosphere was susceptible to moist symmetric instability, the large single band he observed is primarily attributable to frontogenetical forcing which occurred in the absence of a front.

It should be noted that symmetric instability and frontogenesis may not act independently. The condition for ellipticity of the Sawyer–Eliassen equation for transverse frontal circulations is symmetric stability. Emanuel (1985) considered frontogenesis in a symmetrically neutral base state and found that the upward branch of a frontal circulation may be considerably enhanced by low potential vorticity.

In this section the role of frontogenetical forcing is explored through analysis of geostrophic deformation and Q-vector divergence. Fields of geostrophic deformation are used to locate frontogenetically active areas. Divergence of **Q**, the forcing for a three-dimensional Sawyer–Eliassen equation, is used to identify a subsynoptic-scale region of ascent, possibly attributable to frontogenetical forcing.

The geostrophic deformation magnitude and the axis of dilatation are given by

$$|\mathrm{DEF}|_g = [(\partial u_g/\partial x - \partial v_g/\partial y)^2 + (\partial v_g/\partial x + \partial u_g/\partial y)^2]^{1/2}, \quad (1)$$

$$\phi_d = \tan^{-1}\left[\frac{\partial v_g/\partial x + \partial u_g/\partial y}{\partial u_g/\partial x - \partial v_g/\partial y}\right], \quad (2)$$

where ϕ_d is measured counterclockwise from the x-axis and symbols have their usual meanings. If the isotherms form an angle of less than 45° with the axis of dilatation, the deformation is frontogenetical; otherwise it is frontolytical.

Hoskins et al. (1978) derived an equation for w in terms of the forcing function, **Q**:

$$N^2\nabla^2 w + f^2(\partial^2 w/\partial z^2) = 2\nabla\cdot\mathbf{Q}, \quad (3)$$

where

$$\mathbf{Q} = (Q_1, Q_2) = -\frac{g}{\theta_0}(\partial \mathrm{v}_g/\partial x\nabla\theta,\ \partial \mathrm{v}_g/\partial y\nabla\theta). \quad (4)$$

We calculated the fields of deformation and $\nabla\cdot\mathbf{Q}$ in Figs. 5–6 according to these formulae with careful subjective analysis. Arithmetic operations and derivations were approximated by graphically calculated addition, subtraction, and finite differences. Multiplication, division, and trigonometric operations were accomplished with point-by-point calculations at station locations.

Figure 5 shows potential isotherms, geostrophic deformation and dilatation axes at 00 GMT. Maxima in deformation exist over New England at both levels, 850 and 700 mb; geostrophic deformation at 12 GMT (not shown) is weak.

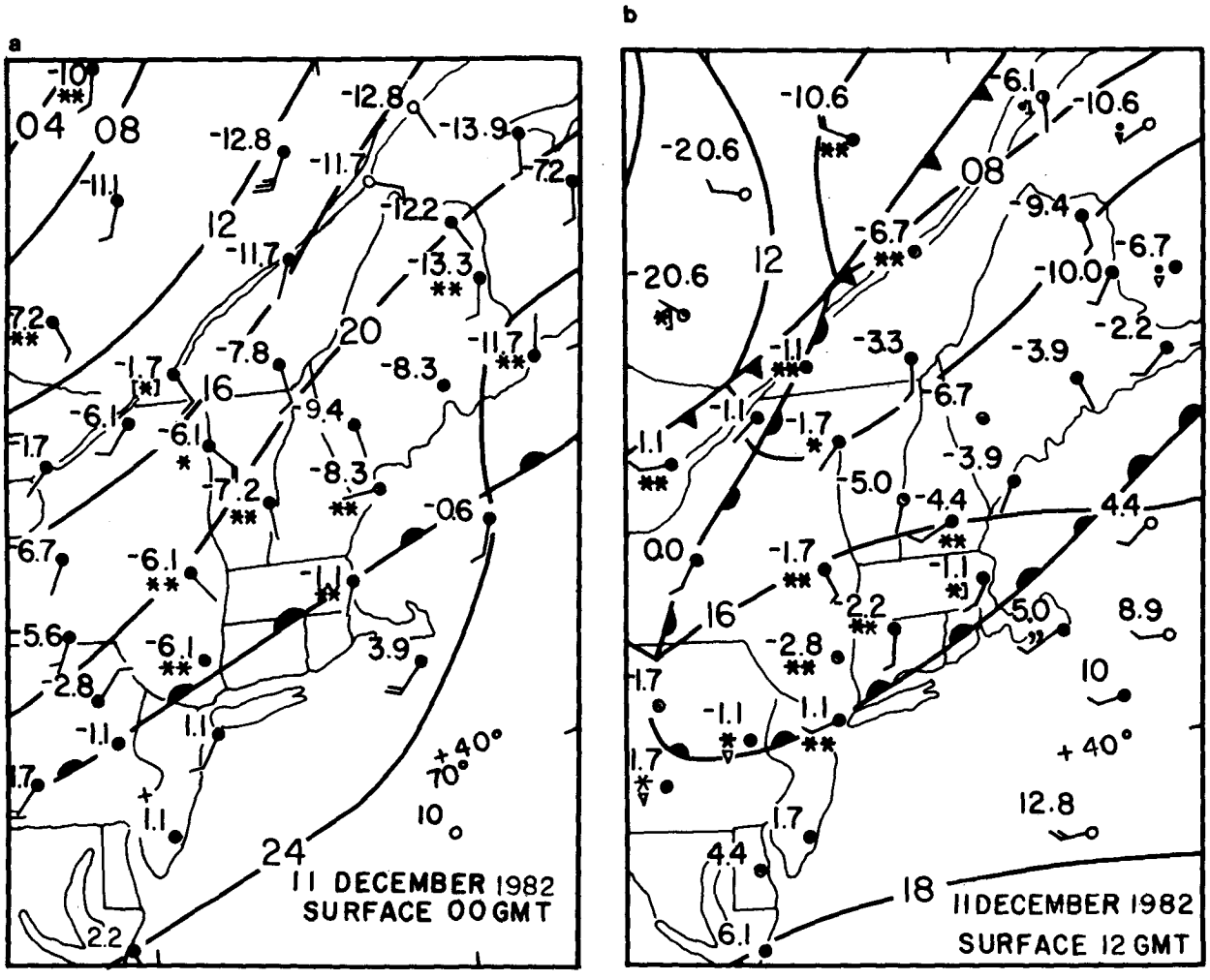

FIG. 3. Surface charts for 11 December 1982 at (a) 00 GMT and (b) 12 GMT. Isobars are shown in solid lines with hundreds and thousands places omitted. Temperatures are in °C.

Figure 6 shows contours of $\nabla \cdot \mathbf{Q}$. Geostrophic frontogenetical forcing of upward motion occurs in regions where $\mathbf{Q}$ is convergent (i.e., $\nabla \cdot \mathbf{Q}$ is negative). The maxima in $|\nabla \cdot \mathbf{Q}|$ correspond roughly to the maxima in geostrophic deformation. The strength of w is estimated by assuming that both terms on the left-hand side of (3) are the same order of magnitude, and that the vertical profile of w takes the form of a sinusoid with zeros at the ground and at 4 km. Then

$$f^2 \frac{\partial^2 w}{\partial z^2} \approx |\nabla \cdot \mathbf{Q}|, \tag{5a}$$

or

$$W \approx \frac{(4 \text{ km})^2}{\pi^2 f^2} |\nabla \cdot \mathbf{Q}|. \tag{5b}$$

If $\nabla \cdot \mathbf{Q} \approx 10^{-15}$ m^{-1} s^{-3}, as suggested by Fig. 6, then,

$$W \approx \frac{(4 \times 10^3 \text{ m})}{\pi^2 (10^{-4} \text{ s}^{-1})^2} 10^{-15} \text{ m}^{-1} \text{ s}^{-3} \approx 0.16 \text{ m s}^{-1}. \tag{6}$$

The scale of the area with positive vertical velocity is larger than the bands. We suggest that this subsynoptic scale ascent could initiate band formation by bringing the atmosphere toward saturation or by lifting parcels to their level of free slantwise convection.

c. *Analysis of radar displays*

Figure 7 shows MIT radar CAPPI displays at 1250 and 1851 GMT. Note that the bands are embedded in the frontogenetically active region discussed previously. Radar displays during the storm indicate that the bands are generally oriented at approximately 60° (clockwise from north) but that there is considerable variability in the size and number of bands present at different times. The bands generally existed as identifiable entities for between one and one-half to four hours. The range-height indicator taken at MIT toward 140° at 0953 GMT (Fig. 8) shows that the reflectivity top was at about 5 km.

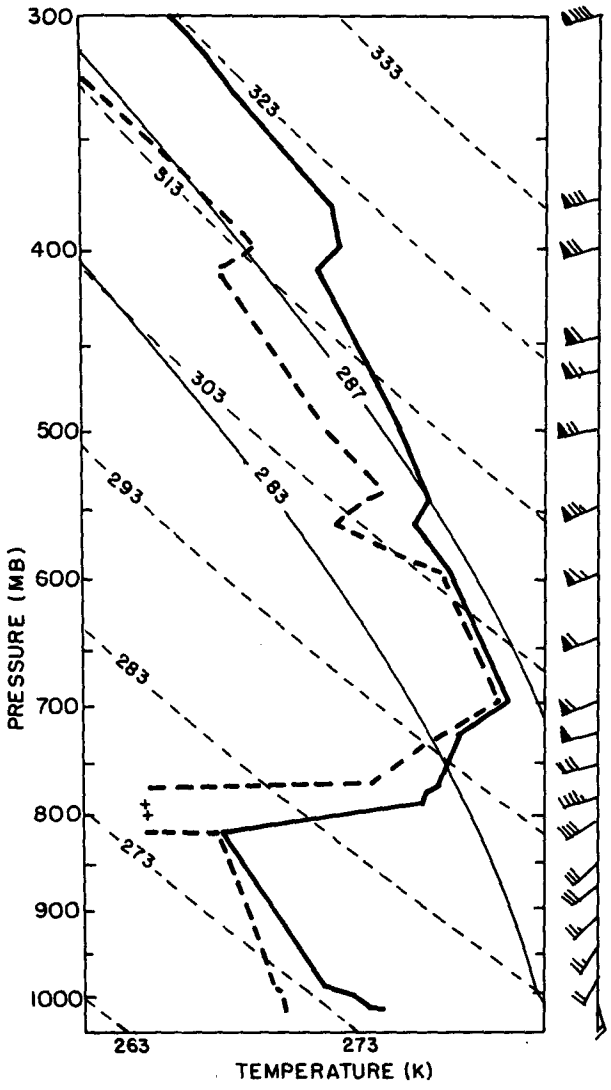

FIG. 4. 00 GMT sounding at Chatham. Atmospheric temperature and dew-point temperature are shown in heavy solid and dashed lines. Reference pseudo-adiabats and moist adiabats are given in light solid and dashed lines. Winds are plotted along the side.

d. Band-normal cross section analysis

Subjectively contoured cross sections of reflectivity and streamfunction (Fig. 9), derived from airplane data, illustrate the airflow and moisture distribution in a plane perpendicular to the band. The x-axis runs normal to the band, increases toward warmer air, and is oriented toward 150°. The y-coordinate is oriented along the band, toward 60°. Figure 7 shows each of the bands during the 725 mb pass with the flight path at 725 mb indicated. The data are projected onto the x-axes of Fig. 9 which are also indicated on Fig. 7. We corrected for motion of the band as discussed in the previous section. The band relative streamlines shown in solid lines on Fig. 9 are calculated by assuming that variations along the band are small. We compared the along-band and cross-band components of divergence with wind measurements from Portland, Chatham and Shelbourne, and Nova Scotia. The along-band divergence is at most one-seventh the magnitude of the across-band divergence, so the assumption of two-dimensionality appears to be justified at large scales. It is also assumed that the wind fields measured by the airplane represent synchronous sets of data. In fact, the flight durations of about one and one-half hours are not particularly short compared to the four-hour life of the morning band or the three and one-third-hour life of the afternoon band. The band relative streamfunction, ψ, is defined as

$$\partial\psi/\partial p = -u, \quad \partial\psi/\partial x = \omega, \tag{7a}$$

with

$$\psi = 0 \quad \text{at} \quad p_{\text{sfc}} = 1022 \text{ mb}, \tag{7b}$$

where u is cross-band wind and $\omega = \dfrac{dp}{dt}$. If $\partial v/\partial y = 0$, (7) exactly satisfies continuity in a hydrostatic flow.

The streamlines of the afternoon flight (Fig. 9b) form a roll circulation, while those of the morning flight (Fig. 9a) suggest but do not confirm such a flow. The airflow in the afternoon flight shows a sloped updraft but the downdraft is not well resolved.

The maximum updraft strengths, calculated by differencing the streamfunction, are -0.12 mb s^{-1} and -0.15 mb s^{-1} in the morning and afternoon flights, respectively. The strongest values of $\partial u/\partial x$ (not shown) are at 815 mb in the morning flight and at 910 mb in the afternoon flight.

The "reflectivity" shown in dashed lines on Fig. 9 is derived from measurements by the 200-Y probe, a one-dimensional optical array probe which sizes and counts hydrometeors with diameters between 300 and 4500 μm, in 15 size categories. In this calculation, a correction was applied to account for the fact that the particles were snow rather than water. It should be noted that such a correction was not applied to data collected by the MIT radar and that the reflectivities shown in the CAPPI displays (Fig. 7) are therefore low by a factor of $[K_w]^2/[K_i]^2 = 0.197/0.93 = -6.7$ dBZ, where K_w and K_i are the indices of refraction for water and ice, respectively.

There are high values of reflectivity, suggesting precipitation particle growth, in the updrafts in Fig. 9. Both the morning and afternoon flights have very low values of reflectivity and relative humidity (not shown) in the return branch of the circulations. (See the lower left corners of the figures.) This dryness may indicate that the downdrafts are unsaturated.

4. Role of symmetric instability

In this section we consider the role of symmetric instability. The moist parcel dynamics model of CSI is briefly reviewed and used to develop criteria for determining when the atmosphere is susceptible to CSI.

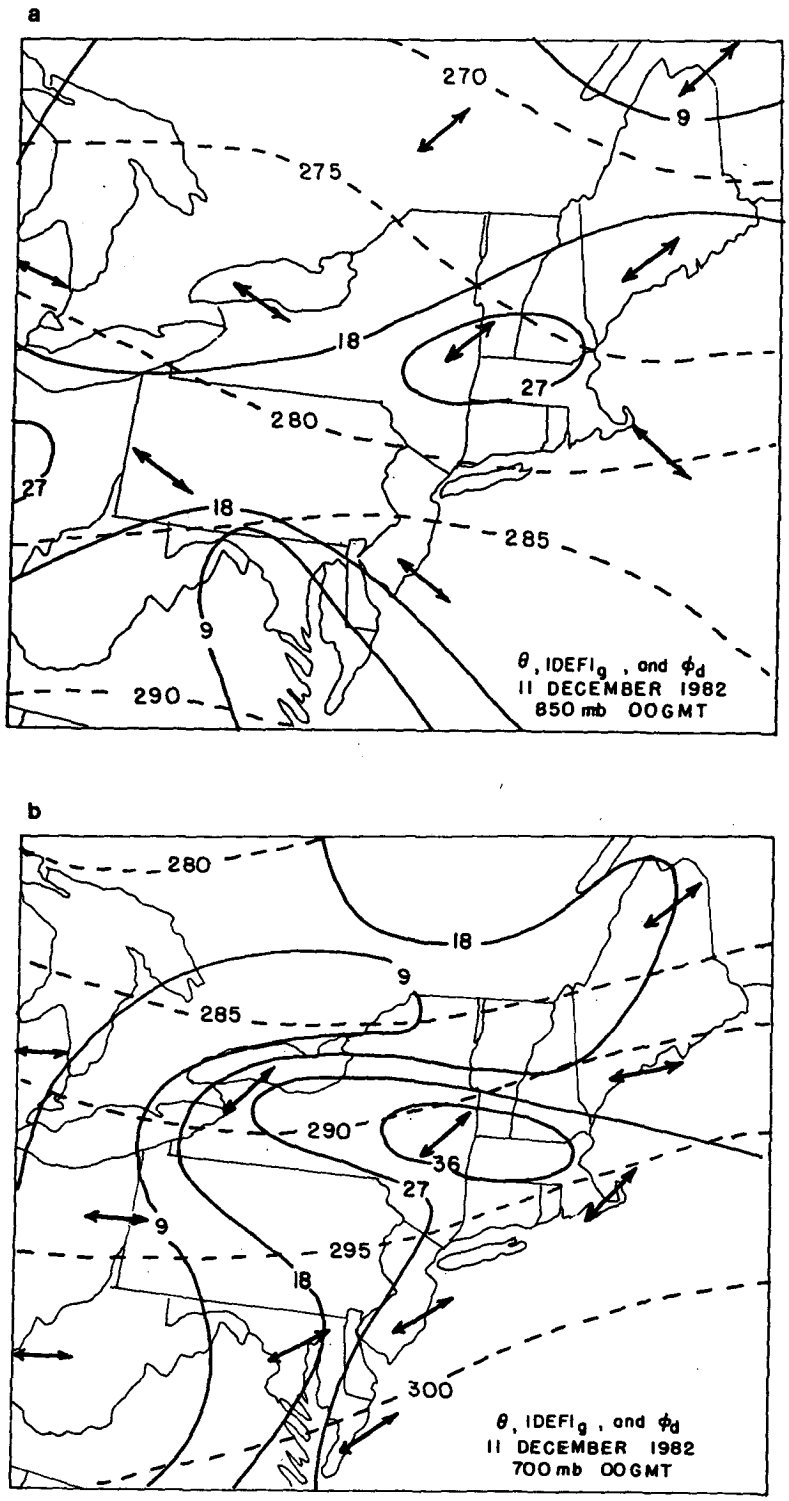

FIG. 5. Geostrophic frontogenetical forcing at 00 GMT for (a) 850 mb and (b) 700 mb. Solid lines are geostrophic deformation in 10^{-6} s^{-1}, dashed lines are potential temperature in K and dilatation axes are shown with double-headed arrows. The deformation is frontogenetical where the isotherms form an angle of less than 45° with the dilatation axes.

These criteria are evaluated with observations and it is shown that the atmosphere is slightly unstable to symmetric instability. Other researchers (Emanuel, 1983b) have suggested that the atmosphere is adjusted to a neutral state as symmetric instability proceeds. However, in this case the atmosphere is unstable at two times, separated by 12 hours, so we postulate that this adjustment process is opposed by a supply of potential energy. By developing and evaluating the terms in an equation for the time rate of change of potential energy, we find evidence that the symmetric instability is sustained by a large-scale process, geostrophic lapse rate advection.

a. The parcel model of moist symmetric instability

Bennetts and Hoskins (1979) and Emanuel (1979) have suggested that some bands which form in layers of stable or neutral thermal stratification, and are imbedded in regions of large-scale ascent, may be caused by symmetric instability. Symmetric instability is manifested in sloped, two-dimensional, mesoscale rolls aligned with the geostrophic shear. The parcel description of moist symmetric instability below closely follows Emanuel (1983b).

We will consider a base state in which a steady, purely meridional flow is in geostrophic balance. In this case, the potential temperature is a function only of x and z, so the thermal wind can be written

$$f\frac{\partial v_g}{\partial z} = \frac{g}{\theta_{v0}}\frac{\partial \theta_v}{\partial x}, \tag{8}$$

where the subscript g denotes the geostrophically and hydrostatically balanced base state.

Suppose a tubular parcel of fluid, extending infinitely in the y direction, is displaced in the x–z plane. The displacement is assumed to proceed slowly so that fields of v_g and θ_v are undisturbed. The parcel equations are

$$\frac{dv_p}{dt} = -fu_p, \tag{9}$$

$$\frac{du_p}{dt} = f(v_p - v_g), \tag{10}$$

$$\frac{dw_p}{dt} = \frac{g}{\theta_{v0}}(\theta_{vp} - \theta_v), \tag{11}$$

where the subscript p refers to the parcel. It can be shown using (9) that a pseudoangular momentum, M, defined as

$$M = v + fx \tag{12}$$

is conserved following the parcel, if the vertical shear is unidirectional. Eq. (10) can be written

$$\frac{du_p}{dt} = f(M_p - M_g). \tag{13}$$

If, after the displacement, the left-hand sides of (11) and (13) have the same sign as the displacement, the parcel will continue accelerating so the displacement is unstable. In particular, slanted displacements may be unstable if the slope of M_g-surfaces are less than those of θ-surfaces. This criterion is illustrated in the papers cited previously. If the environment is saturated, θ_e should be substituted for θ to account for release of latent heat. If the environment is moist but not saturated, while the parcel is saturated, a quantity S is introduced; S is defined as a surface along which a particular parcel has neutral buoyancy. A possible configuration of M_g and S is given in Emanuel (1983a).

b. Evaluation of susceptibility to symmetric instability

The atmosphere's susceptibility to symmetric instability can be evaluated with cross sections across the mean vertical shear as previously discussed. In this case, the best cross section is a line through the upper air stations along the East Coast as indicated in Fig. 1. The cross section is at an angle of about 30° to the shear normal direction. The distance used in calculating $M_g = v_g + fx$ is the projection of the physical distance between the stations onto an axis perpendicular to the mean shear vector; v_g is the component of the geostrophic velocity along the mean shear.

Figure 10 shows cross sections of θ_e and M_g. Regions in which the slopes of M_g-surfaces are less than or equal to the slopes of θ_e-surfaces are shaded. Note the very statically stable layer which slopes from the surface at Wallops Island, Virginia, to about 3 km at Caribou, Maine, in both figures. It is clearly associated with the fronts discussed in Section 2. The inversion caps any vertical motions which might develop near the surface.

At 00 GMT (Fig. 10a), the major region of instability is between 3 and 4 km and extends from Providence, Rhode Island, to Augusta, Maine. At 12 GMT (Fig. 10b), the shaded region is from 3 to 5 km deep and extends from Atlantic City, New Jersey, to Augusta. It should be recalled that the instability criterion stipulating that M_g-surfaces be less steep than θ_e-surfaces pertains to saturated air. The shaded regions, therefore, may not necessarily be unstable regions except for parcels originating in the cloudy air.

c. Slantwise potential energy

The potential energy released as a result of a slantwise displacement is the path integral of the forces in (11) and (13). The potential energy, or the slantwise positive area (SPA), given by Emanuel (1983a) is

$$\text{SPA} = \int_{\text{LFC}}^{\text{LNB}} \left[f(M_p - M_g)\mathbf{i} + \frac{g}{\theta_{v0}}(\theta_{vp} - \theta_{vg})\mathbf{k} \right] \mathbf{ds} \tag{14}$$

where the LNB and LFC are the level of neutral buoy-

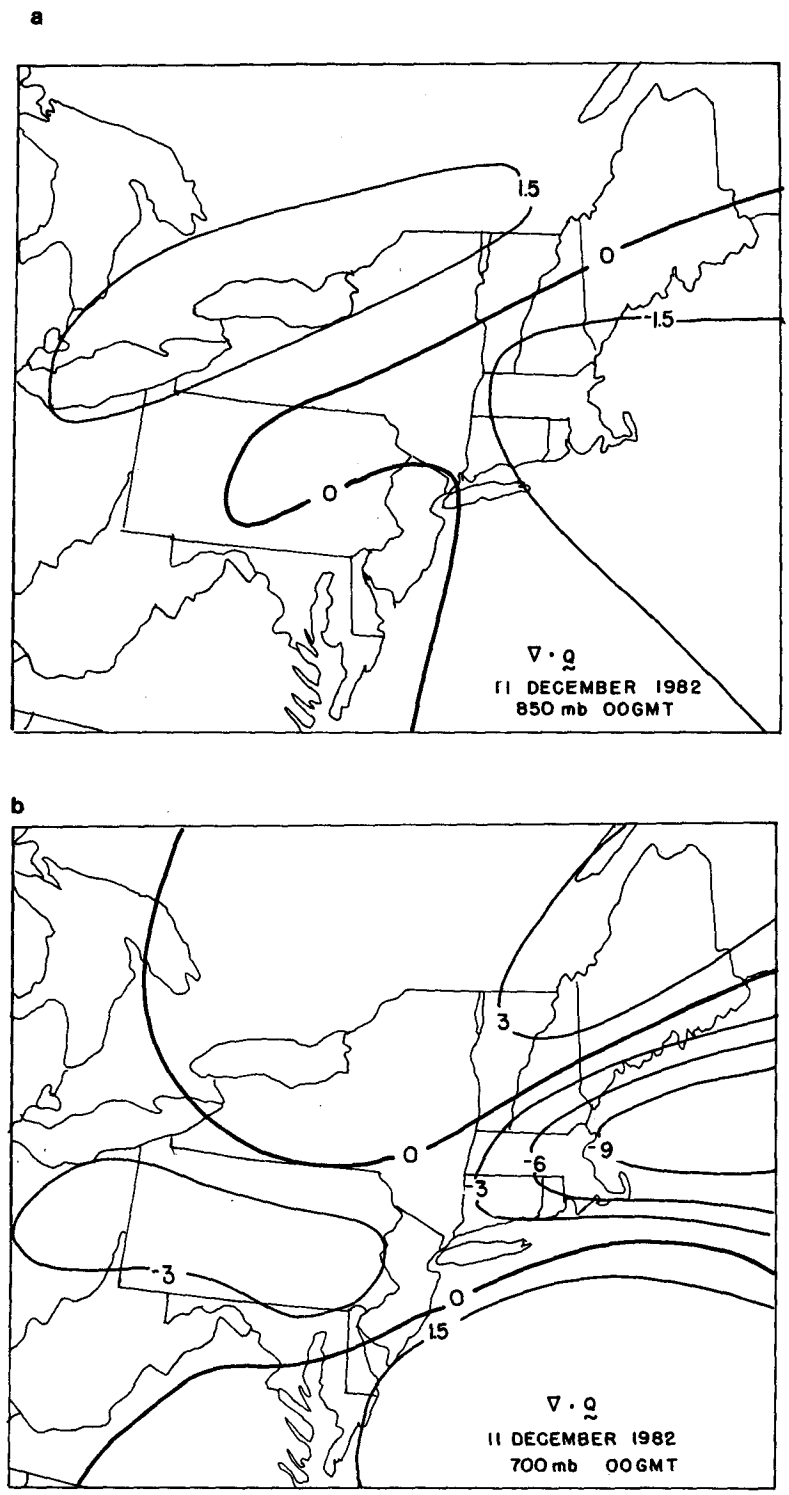

FIG. 6. Values of $\nabla \cdot \mathbf{Q}$ in 10^{-16} s^{-3} m^{-1} at (a) 850 mb at 00 GMT, (b) 700 mb at 00 GMT, (c) 850 mb at 12 GMT, and (d) 700 mb at 12 GMT. Upward motion is associated with convergent **Q**.

ancy and the level of free convection, respectively, as defined in Emanuel (1983a). We assume in evaluating (14) that the parcel is positively buoyant at some level.

The curl of the integrand is zero by the thermal wind relation as shown in Emanuel (1983a). Thus the integral is path independent. If Eq. (14) is evaluated along

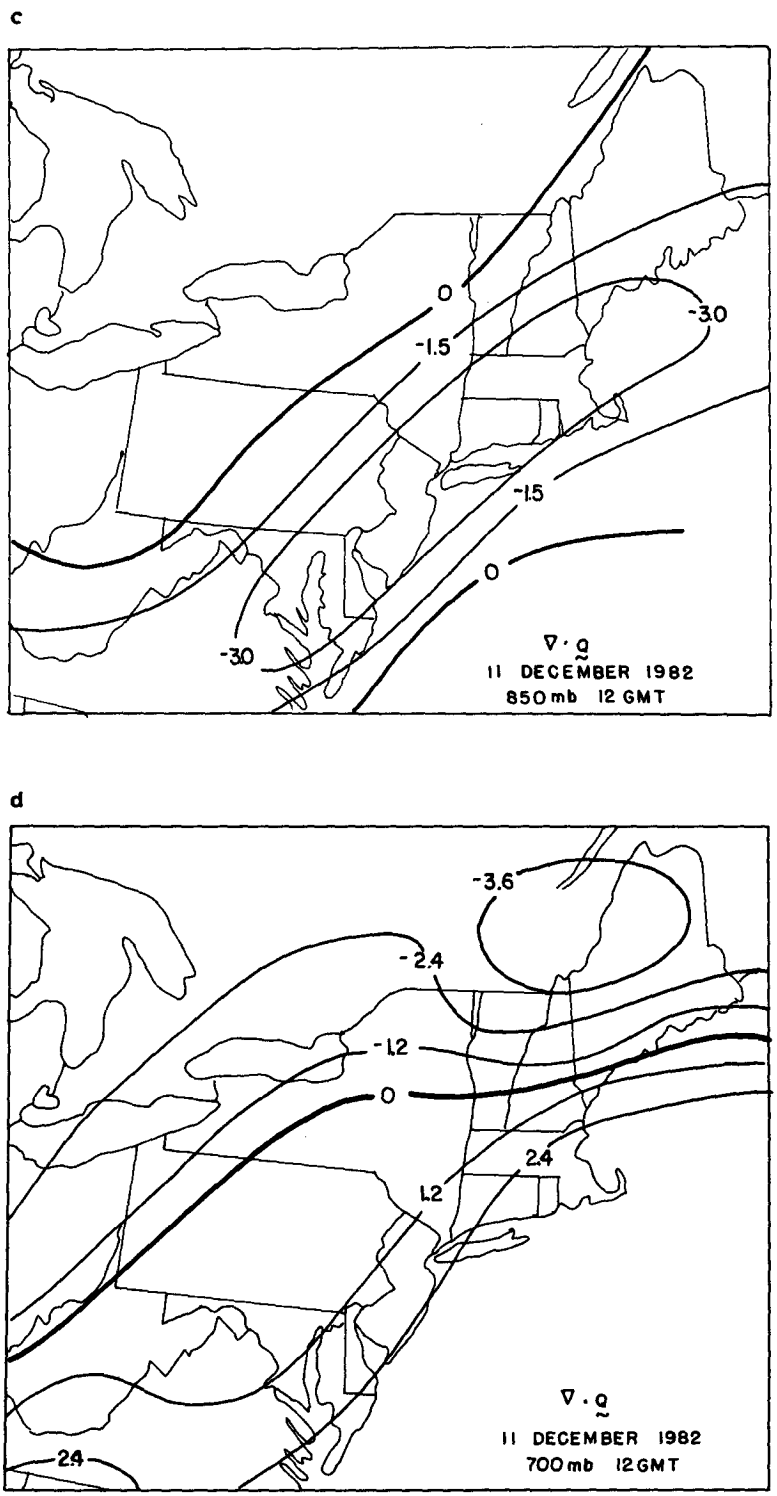

FIG. 6. (*Continued*)

an M_g-surface, the first term of the integrand drops out, so

$$\text{SPA} = \int_{\text{LFC}}^{\text{LNB}} \left|_{M_g} \frac{g}{\theta_{v0}} (\theta_{vp} - \theta_{vg}) dz. \right. \tag{15}$$

The SPA can be evaluated as described in Emanuel (1983b) by constructing a vertical cross section of M_g, θ, and dew point temperature (T_D) surfaces. The values of θ and T_D are thus interpolated along an M_g surface,

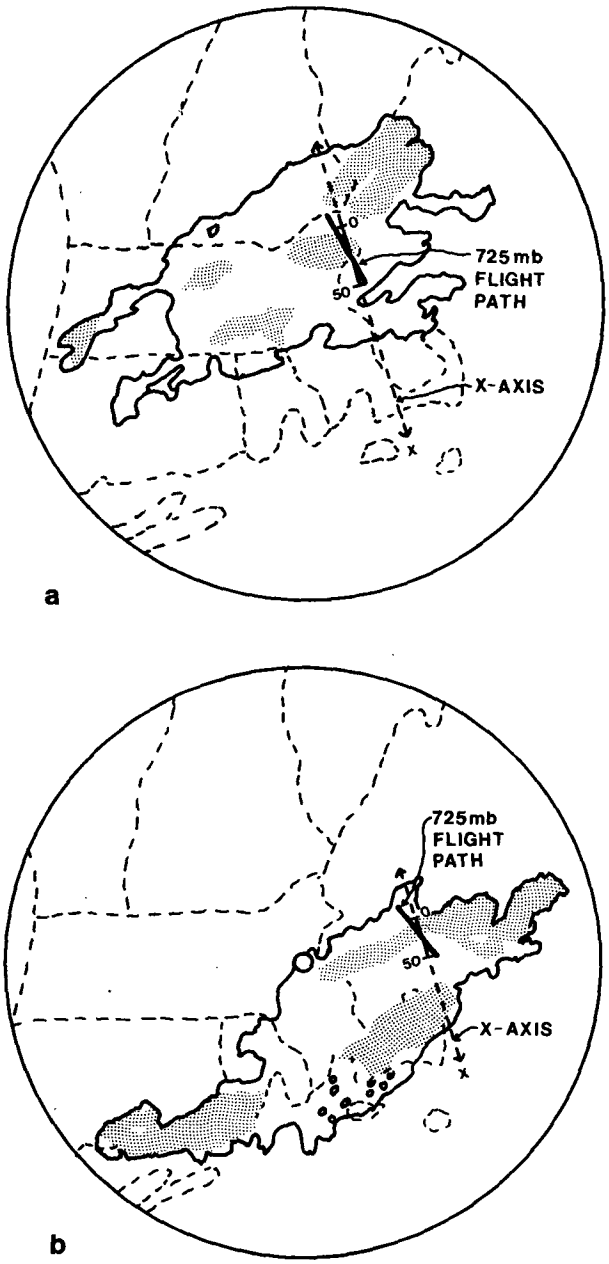

FIG. 7. Displays of CAPPI radar reflectivity between 2.5 and 4.0 km at (a) 1250 GMT and (b) 1851 GMT. Solid lines show contours of minimum detectable reflectivity. Regions with strong reflectivity are shaded. Airplane flight paths at 725 mb and x-axes for the band-normal cross sections in Fig. 9 are indicated.

plotted on a tephigram, and SPA is evaluated in the standard manner.

It should be noted that two assumptions made in defining the base state are violated by observations previously discussed. First, the vertical shear turns with height, so M_g is not strictly conserved. It may be asked if SPA is a relevant physical quantity in this case, but we shall proceed as if it were. That is, we assume that the angle of shear variation is small and that (13) is a good approximation.

The other violated assumption is that of a geostrophically balanced base state. We evaluate symmetric instability using the geostrophic winds because the pressure gradient balancing a displaced parcel is probably best represented by fv_g.

d. *Evaluation of slantwise potential energy*

Soundings of θ and T_D along $M_g = -10$ m s^{-1} are constructed from cross sections of M_g, θ, and T_D (not shown). The 00 GMT sounding is shown in Fig. 11, plotted on a skew T-log p chart. If the most unstable parcels are lifted to achieve the greatest difference between parcel and environmental potential temperature, there are approximately 4° of buoyancy.

Soundings from the morning cross section (not shown) also show 3 to 4° of buoyancy. It should be noted, however, that the M_g-surfaces are practically horizontal in the unstable regions and that parcels would have to travel hundreds of kilometers to actually achieve the maximum buoyancy. A reasonable estimate of the buoyancy a parcel might acquire is probably closer to 1 K.

e. *Time rate of change of SPA*

It is instructive to evaluate some measure of how the available energy for slantwise convection changes with time. For this purpose, we assume that at a given time the SPA is positive and evaluate its time rate of change following the particular parcel for which the SPA is defined. First, as a matter of convenience, we note, following Emanuel (1983a), that since M_g-surfaces are vertical in geostrophic coordinates (e.g., see Hoskins, 1975), the integral in (15) is a simple vertical integral in those coordinates:

$$\text{SPA} = \int_{\text{LFC}}^{\text{LNB}} \frac{g}{\theta_{v0}} (\theta_{vp} - \theta_{va}) dZ, \qquad (16)$$

where θ_{vp} is understood to be the virtual potential temperature of a parcel lifted from below its LFC and θ_{va} is simply the ambient virtual potential temperature. It

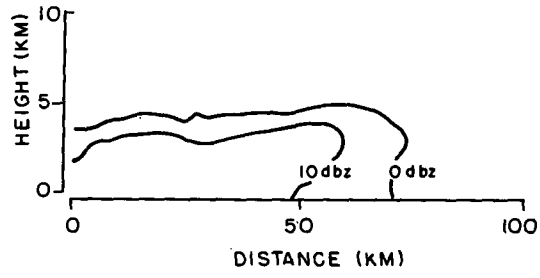

FIG. 8. Range Height Indicator display taken at 0953 GMT from MIT toward 140°.

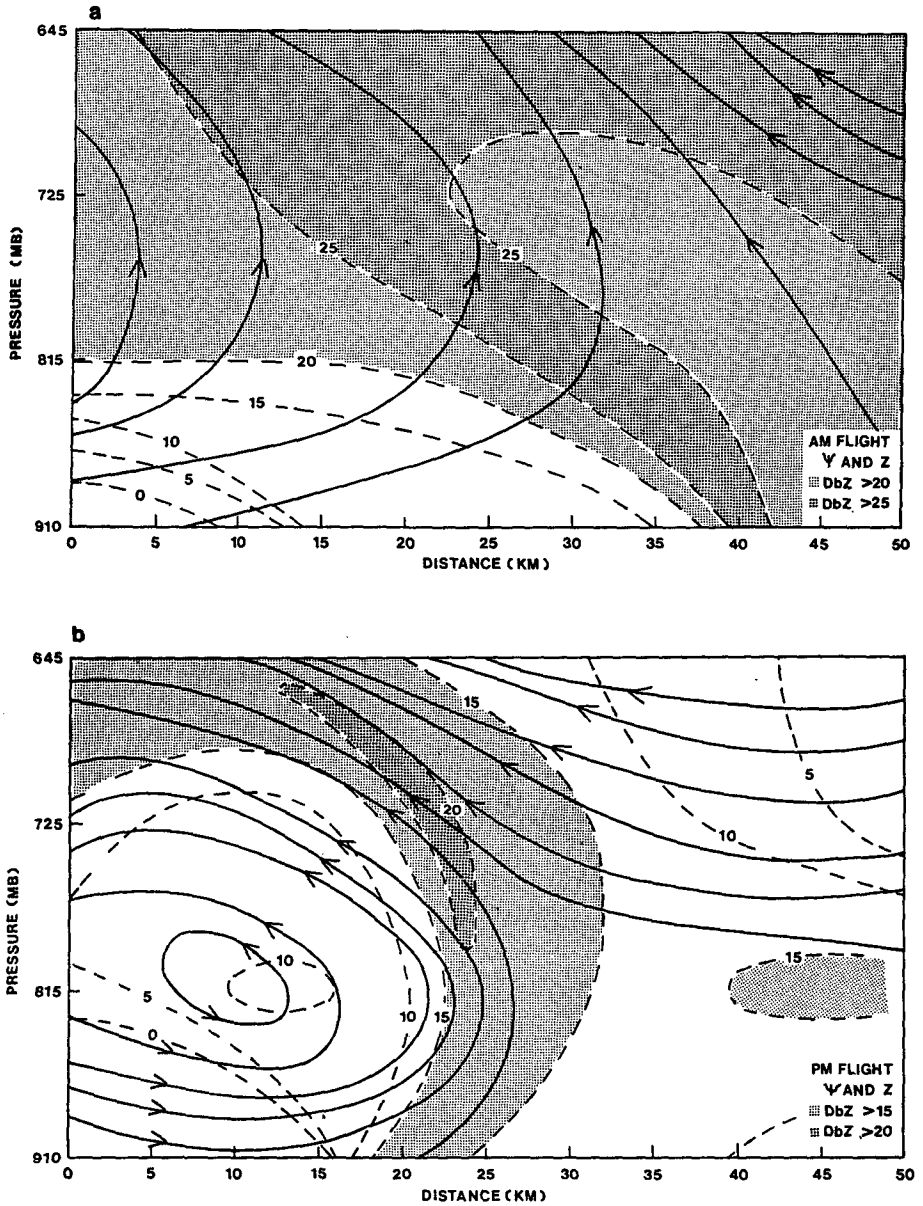

FIG. 9. Band-normal cross sections showing band-relative streamlines in solid lines every 250 mb m s^{-1} and reflectivity in dashed lines in dBZ for (a) the 1230 GMT flight and (b) the 1830 GMT flight. The airplane flew at the pressure levels labeled on the ordinate. These cross sections correspond to the bands shown in Fig. 7.

is understood that the integral is evaluated at fixed X and Y, where

$$X = x + v_g/f, \tag{17a}$$

$$Y = y - u_g/f, \tag{17b}$$

$$Z = z, \tag{17c}$$

$$\Phi = \phi + \frac{1}{2}(u_g^2 + v_g^2), \tag{17d}$$

where X, Y and Z are the geostrophic coordinates, ϕ is the geopotential in physical coordinates and Φ is the geostrophic geopotential.

Now define a coordinate system moving with the parcel by whose vertical displacement we evaluate the SPA. The time rate of change, $(\partial/\partial\tau)$, of SPA in this coordinate system is

$$\frac{\partial}{\partial\tau}\,\mathrm{SPA} = \frac{\partial}{\partial\tau}\int_{\mathrm{LFC}}^{\mathrm{LNB}} \frac{g}{\theta_{v0}}(\theta_{vp} - \theta_{va})dZ$$

$$= \int_{\mathrm{LFC}}^{\mathrm{LNB}} \frac{g}{\theta_{v0}}\left(\frac{\partial\theta_{vp}}{\partial\tau} - \frac{\partial\theta_{va}}{\partial\tau}\right)dZ. \tag{18}$$

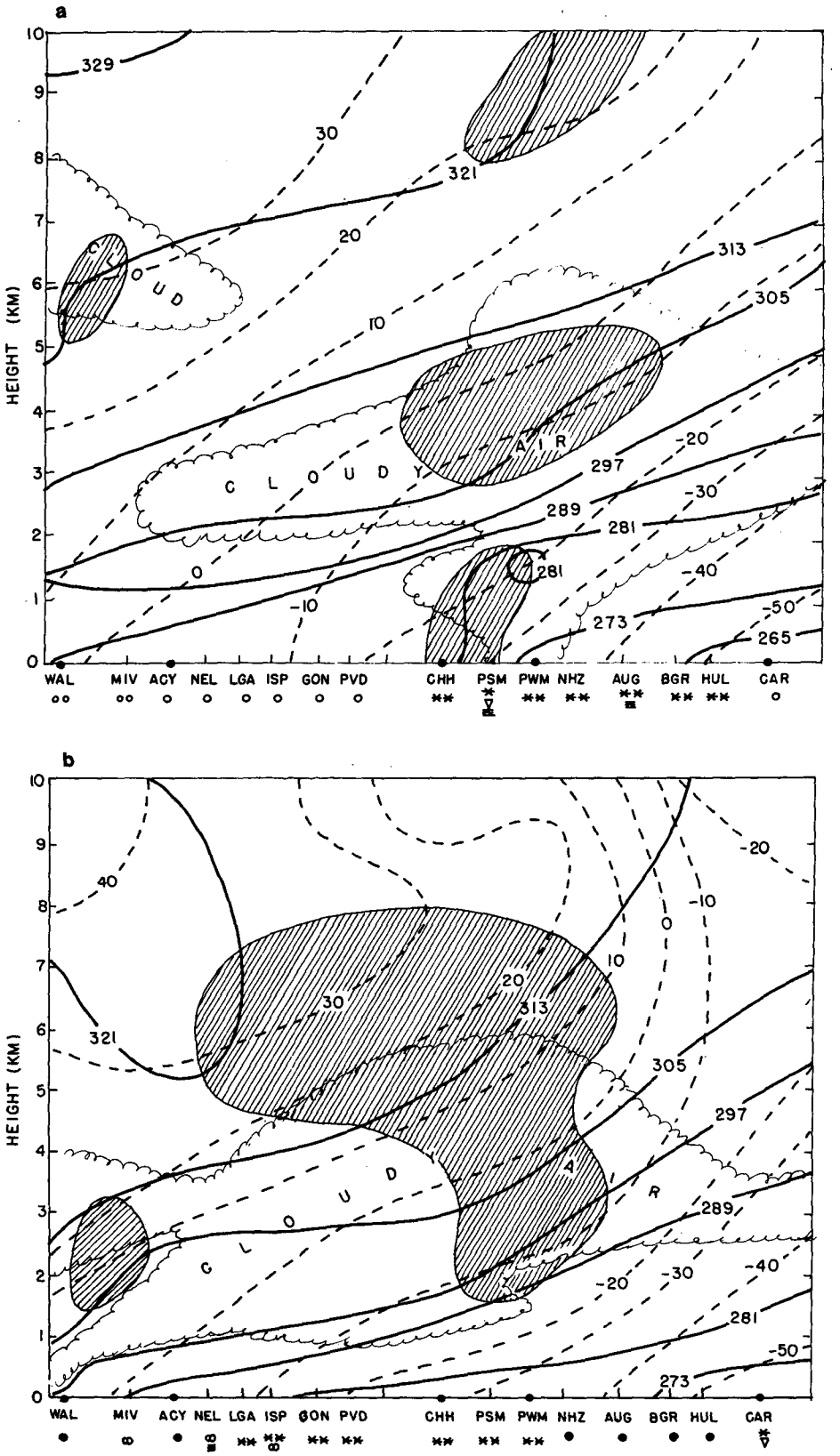

FIG. 10. Vertical cross sections of θ_e in K (solid lines) and M_g in m s^{-1} (dashed lines) at (a) 00 GMT and (b) 12 GMT. Clouds are indicated with scalloped lines and regions of possible conditional symmetric instability are shaded. Upper air stations are indicated on the abscissa with large dots. Weather observed at surface stations is indicated below the axis (** = light snow, oo = light rain, ∇ = showers, ≡ = fog, ● = skies overcast, O = skies broken and ∞ = haze).

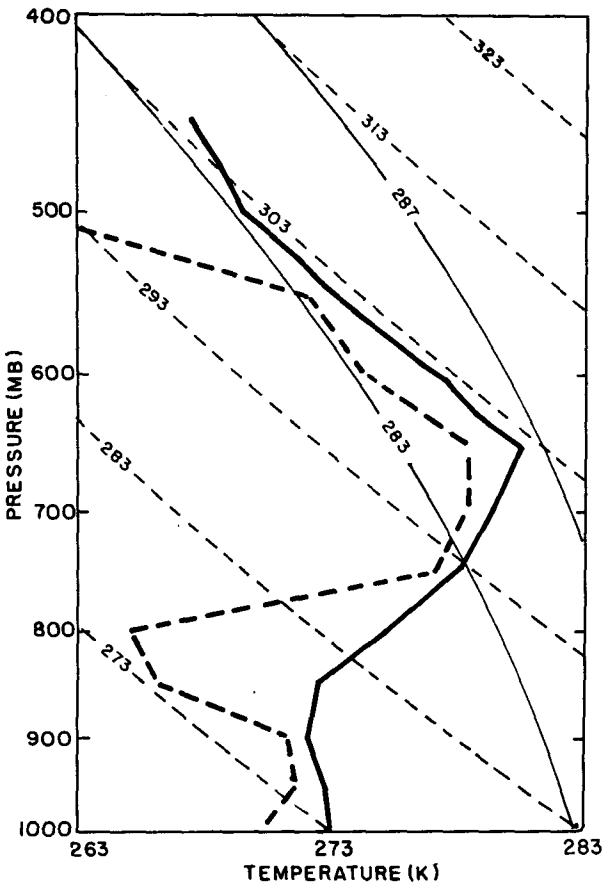

FIG. 11. Sounding along $M_g = -10$ m s^{-1} at 00 GMT. Potential temperatures and dew points were interpolated along the M_g-surface shown in Fig. 10a. Positive area can be interpreted as potential energy for displacements along the M_g surface.

The latter relation is obtained because the integrand vanishes by definition at the end points of the integration.

In this coordinate system, the time rate of change of the parcel's lifted temperature is simply related to the rate of heating of the parcel; it is the rate at which the moist adiabat associated with the parcel moves to the left or right on a tephigram. It is shown in the Appendix that (18) can be written as

$$\frac{\partial}{\partial \tau}\,\mathrm{SPA} = \dot{H}_p \frac{T_{\mathrm{LFC}} - T_{\mathrm{LNB}}}{T_p} + \int_{\mathrm{LFC}}^{\mathrm{LNB}} \left[\frac{g}{\theta_0}(\mathbf{V}_{ga} - \mathbf{V}_{gp})\cdot \nabla_X \theta_a + W_a q_a\right] dZ, \quad (19)$$

where

$$q_a = \begin{cases} \dfrac{g}{\theta_0}\dfrac{\partial \theta_a}{\partial Z} & \text{for unsaturated environment} \\ \dfrac{g}{\theta_{ea}}\dfrac{\Gamma_m}{\Gamma_d}\dfrac{\partial \theta_e}{\partial Z} & \text{for saturated environment.} \end{cases}$$

Here, $\dot{H}_p$ is the total sensible and latent heating of the parcel to be lifted ($\dot{H}_p = C_p T_p \partial \ln \theta_{ep}/\partial \tau$) and T_{LFC}, T_{LNB}, and T_p are the absolute temperatures at the lifted condensation level, the level of neutral buoyancy, and the parcel origin level, respectively. The subscripts p and a refer to the origin level of the parcel and the ambient environment, respectively, while the subscript X on the gradient operator indicates a gradient in geostrophic coordinates. The quantity q_a represents the effective static stability in geostrophic coordinates with Γ_m and Γ_d denoting the moist and dry adiabatic lapse rates, respectively.

The processes which can change SPA, according to (19), are 1) real heating of the parcel with respect to which the SPA is defined [first term on right of (19)], 2) geostrophic lapse rate advection, and 3) dry or moist adiabatic warming or cooling of the environment.

Geostrophic lapse rate advection, which is given by the first term in the integrand, can be written

$$(\mathbf{V}_{ga} - \mathbf{V}_{gp})\cdot \nabla_X \theta_a = \frac{g}{f\theta_0}(Z - Z_p)(\overline{\nabla_X \theta} \times \nabla_X \theta)\cdot \mathbf{k}, \quad (20)$$

where

$$\mathbf{V}_{ga} - \mathbf{V}_{gp} = \left(\mathbf{k} \times \frac{g}{f\theta_0}\overline{\nabla_X \theta}\right)(Z - Z_p), \quad (21)$$

through the thermal wind relation and

$$\overline{\nabla_X \theta} \equiv \frac{1}{Z - Z_p}\int_{Z_p}^{Z} \nabla_X \theta\, dZ, \quad (22)$$

where Z_p is the parcel level. The right-hand side of (20) is zero if the geostrophic shear does not turn with height and is greater than zero if it turns counterclockwise with height in the Northern Hemisphere. If the right-hand side of (20) is positive, SPA is increased due to the advection of steeper lapse rates by the geostrophic wind. That is, the upper atmosphere becomes colder with respect to a parcel lifted along an M_g surface.

f. Evaluation of depletion and generation of SPA

In this subsection we attempt to use observations to determine which of the processes previously discussed are important. First, we will estimate how much potential energy is lost through overturning by assuming that some of the potential energy, which is converted to kinetic energy, is dissipated by turbulence. Since buoyancy is released by vertical motions, an appropriate time scale is $T = H/W$ where $H \sim 2$ km, the vertical extent of the band, and $W \sim 0.4$ m s^{-1}, an average updraft observed in the band; H may be thought of as a mixing length. The buoyancy, B, is defined as $B = (g/\theta_0)\Delta\theta$, where $\Delta\theta$, the difference between the environmental and parcel potential temperature, is taken to be 1 K.

The depletion of SPA may then be estimated as the time rate of change of buoyancy, integrated along an M_g-surface:

$$\int \frac{dB}{dt}\,dZ \approx \frac{B}{T}H \approx \left(\frac{9.8\ \text{m s}^{-2}}{288\ \text{K}}\right)(1\ \text{K})\left(\frac{0.4\ \text{m s}^{-1}}{2\ \text{km}}\right) \times (2\ \text{km}) \approx 0.014\ \text{m}^2\ \text{s}^{-3}. \quad (23)$$

This figure will be taken as the rate of SPA depletion due to band scale and sub-band scale motions. Since we observed that new bands continued to form for a period of almost 24 hours in spite of this depletion, we postulate that there must have been some source of potential energy. In the previous subsection, we determined which processes can change SPA. The second of these, geostrophic lapse rate advection, occurs when the geostrophic shear backs with height.

Figure 12 shows that the geostrophic shear at Chatham backs with height between 850 and 500 mb at 00 GMT and between 850 and 300 mb at 12 GMT. Geostrophic lapse rate advection can thus contribute to the SPA rate equation. The magnitude of this effect, which is given by (22), is estimated by transforming constant pressure maps into semigeostrophic coordinates according to (19). Figure 13 shows semigeostrophic maps of potential temperature and $\Delta\Phi$, the thickness in semigeostrophic geopotential of the layer between 850 and 500 mb. The thermal wind, which is roughly the pressure-weighted shear, flows along contours of $\Delta\Phi$. There is positive contribution to (20) in regions where the local temperature gradient along the mean thermal wind is positive. The temperature increases in the direction of the mean thermal wind in most regions on Fig. 13, so GLRA increases SPA.

A typical value of the vector difference $|\mathbf{V}_p - \mathbf{V}_a|$ is 25 m s^{-1}, where $\mathbf{v}_p$ is evaluated at 850 mb and $\mathbf{v}_a$ is evaluated at 500 mb. A typical value of $\nabla_X\theta_a$, the semigeostrophic temperature gradient in the direction of $(\mathbf{v}_p - \mathbf{v}_a)$, evaluated at 500 mb, is 2.5 K in 100 km. The thickness of the layer between 850 and 500 mb, H, is about 4 km. By (23), the increase in SPA due to GLRA is estimated as

$$\frac{\partial}{\partial\tau}\text{SPA} \approx \frac{g}{\theta_0}|\mathbf{V}_{g850} - \mathbf{V}_{g500}|\nabla_X\theta\, H \approx \frac{9.8\ \text{m s}^{-2}}{288\ \text{K}}(25\ \text{m s}^{-1}) \times (2.5\times10^{-5}\ \text{K m}^{-1})(4\times10^{3}\ \text{m}) \approx 0.09\ \text{m}^2\ \text{s}^{-3}. \quad (24)$$

This value is larger than the rate of depletion estimated in (23). It therefore appears that geostrophic lapse rate advection produces an ample supply of potential energy.

The other two processes which can affect SPA, real heating of the parcel and adiabatic warming or cooling of the environment, appear to be unimportant in this case. The stable frontal layer apparent on soundings (e.g., Fig. 4) and vertical cross sections (Fig. 10) probably prevented any parcels in recent contact with the surface from participating in the convection. Trajectory analyses indicate that parcels which might have been warmed by the ocean moved to the northeast and did not circle back inland.

The third of the processes, adiabatic warming or cooling of the environment, acted to decrease SPA in this case. Positive vertical velocity in unstable regions of the atmosphere has the effect of warming the environment because $\partial\theta/\partial Z$ is negative along M_g surfaces in these regions. The ambient vertical velocity, estimated above, is $w_a \sim 0.1$ m s^{-1} and $\partial\theta/\partial Z \sim 0.1$ K km^{-1}. Thus the magnitude of adiabatic warming of the environment can be roughly estimated from (19):

$$\frac{\partial}{\partial\tau}\text{SPA} \approx \frac{g}{\theta_0}w_a\frac{\partial\theta}{\partial Z}H \approx \left(\frac{9.8\ \text{m s}^{-2}}{288\ \text{K}}\right)(-0.1\ \text{m s}^{-1}) \times (10^{-4}\ \text{K m}^{-1})(2\times10^{3}\ \text{m}) \approx -7\times10^{-4}\ \text{m}^2\ \text{s}^3. \quad (25)$$

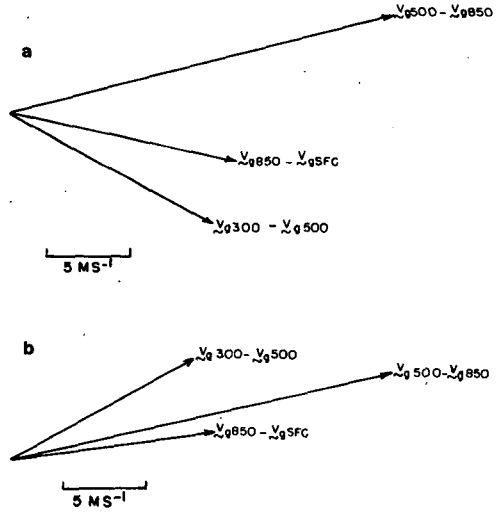

FIG. 12. Rotation of the geostrophic shear vector at Chatham at (a) 00 GMT and (b) 12 GMT.

5. Discussion and conclusions

Symmetric instability may explain many observed features of the bands in this case. Substantial portions of the atmosphere were conditionally unstable according to the criteria of the parcel model of moist conditional symmetric instability in two-dimensional flow. The bands formed in the unstable layers. Bands took the form of sloped rolls almost parallel to the mean shear, as predicted by the theory.

A few observations remain unexplained. The slope of the displacement is expected to be intermediate between the slopes of the M_g- and θ_e-surfaces. However, the streamlines found in the airplane band-normal

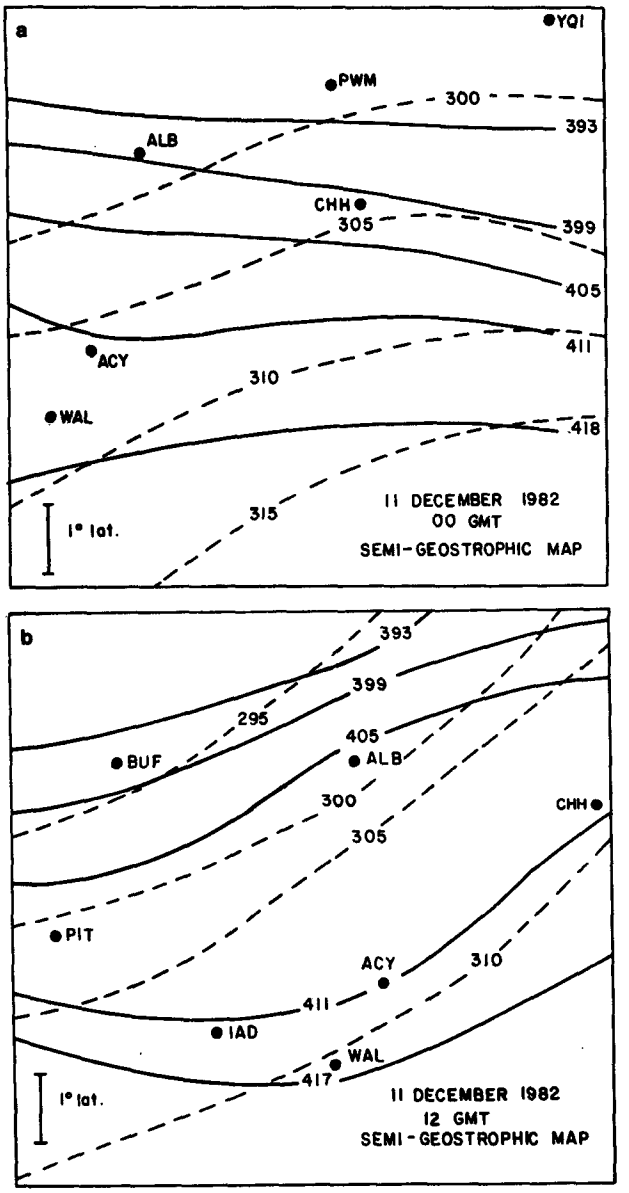

FIG. 13. Semigeostrophic maps of difference in semigeostrophic geopotential between 500 and 850 mb (solid lines) and potential temperature at 500 mb (dashed lines) at (a) 00 GMT and (b) 12 GMT. Station locations in semigeostrophic coordinates at 850 mb are shown for reference. Slantwise positive area is increased by the geostrophic wind advecting steeper lapse rates, with respect to a parcel at 850 mb, in regions where the potential temperature increases in the direction of the mean thermal wind which flows along contours of $\Delta\Phi$.

cross sections were steeper than either the M_g- or θ_e-surfaces. The current model does not explain the different numbers of bands observed at various times. Time-dependent behavior in the rolls was sometimes observed on movies made from series of CAPPI displays. The stability of two-dimensional rolls to smaller perturbations is not known.

The rate at which potential energy was generated and converted to kinetic energy was estimated. The rate of potential energy generation appears to have been greater than the rate of its dissipation. However, the conditions for symmetric instability were derived under the assumption of two-dimensional flow. The counterclockwise rotation of the shear vector, which led to SPA generation by geostrophic lapse rate advection, violates this assumption.

A region of subsynoptic scale ascent was attributed to frontogenetical forcing. This intermediate-scale process could have contributed to formation of bands by bringing the atmosphere to saturation and lifting conditionally unstable parcels to their lifting condensation level. The relation between frontogenetical forcing and band formation is highlighted by the fact that the bands became smaller and weaker as the warm front diffused during the later periods of the case study. The progressive decrease in band width and strength did not seem to be related to parameters relevant to symmetric instability, such as vertical shear or stratification. The ageostrophy, apparently attributable to frontogenesis, also results in a base state which violates conditions under which symmetric instability has been derived.

The degree to which observed band characteristics correspond to predictions of symmetric instability suggests that the results of the theory have some relevance even when there are deviations from the idealizations. Future analytical work and numerical simulations should address the hypothesis that three-dimensional and ageostrophic base states may be symmetrically unstable. The effect of the former condition is particularly relevant because it allows generation of energy for the instability.

Acknowledgments. This work was performed under support from NSF Grant ATM-8209375. Thanks are due to Dr. Frederick Sanders, Mr. Stephen Garner, and Mr. Peter Neilley for insightful discussion and assistance in taking the data. Some of the work was completed while one of the authors (DGW) was at Los Alamos National Laboratory. The authors thank Dr. Douglas Lilly and Dr. Tzvi Gal-Chen for support during completion of the final manuscript. We are grateful to Isabelle Kole and Kathy Kanak for drafting the figures and to Vicky Hall and Ginger Rollins for typing the manuscript.

APPENDIX

Derivation of an Equation for the Rate of Change of Slantwise Positive Area

To facilitate the derivation of (19), we slightly redefine the SPA so that it exactly represents the available energy for a reversibly lifted parcel. We first note that a reversibly lifted parcel will be associated with a density anomaly but not a pressure anomaly. We can then write the horizontal momentum equation for the parcel as

$$\frac{du_p}{dt} = -\alpha_a \frac{\partial p}{\partial x} - (\alpha_p - \alpha_a)\frac{\partial p}{\partial x} + fV_p$$

$$= f(V_p - V_g) - \frac{\alpha_p - \alpha_a}{\alpha_a} fV_g$$

$$= f(M_p - M_g) - \frac{\alpha_p - \alpha_a}{\alpha_a} fV_g, \qquad \text{(A1)}$$

where α is the specific volume (including effects of water vapor). Similarly, the vertical acceleration of the parcel is given by

$$\frac{dw_p}{dt} = \frac{\alpha_p - \alpha_a}{\alpha_a} g. \qquad \text{(A2)}$$

Now the SPA is defined as the line integral of the force per unit mass:

$$\text{SPA} \equiv \int \left(\frac{du_p}{dt}\mathbf{i} + \frac{dw_p}{dt}\mathbf{k}\right)\cdot d\mathbf{l},$$

where $\mathbf{i}$ and $\mathbf{k}$ are unit vectors in the x and z directions, respectively. Using (A1) and (A2) it becomes

$$\text{SPA} = \int \left[f\left(M_p - M_g - \frac{\alpha_p - \alpha_a}{\alpha_a} V_g\right)dx + \frac{\alpha_p - \alpha_a}{\alpha_a} g dz\right]. \qquad \text{(A3)}$$

It is easily demonstrated from the thermal wind relation that the curl of the integrand vanishes, so that the choice of integration path is immaterial. As in Emanuel (1983a), we choose the path to lie along an M_g surface with the limits of integration at the parcel's LFC and LNB. Then (A3) becomes

$$\text{SPA} = \int_{\text{LFC}}^{\text{LNB}} \Big|_M \left(\frac{\alpha_p - \alpha_a}{\alpha_a}\right)(-fV_g dx + g dz), \qquad \text{(A4)}$$

where it is understood that the path of integration lies along an M_g surface. Now since

$$dp = \frac{\partial p}{\partial x} dx + \frac{\partial p}{\partial z} dz = \frac{fV_g}{\alpha_a} dx - \frac{g}{\alpha_a} dz,$$

(A4) can be written

$$\text{SPA} = \int_{\text{LFC}}^{\text{LNB}} \Big|_M -(\alpha_p - \alpha_a)dp. \qquad \text{(A5)}$$

Since, by definition, $\alpha_p = \alpha_a$ at the LFC and LNB, the time derivative following the parcel to be lifted is

$$\frac{\partial}{\partial \tau}\text{SPA} = \int_{\text{LFC}}^{\text{LNB}} \Big|_M -\left(\frac{\partial \alpha_p}{\partial \tau} - \frac{\partial \alpha_a}{\partial \tau}\right)dp. \qquad \text{(A6)}$$

We next note that the lifted parcel is saturated between its LFC and LNB. The lifted parcel's specific volume, α_p, may be regarded as a function of any two state variables. In this case, we regard α_p as a function of moist entropy, s^*, and pressure. Then at each pressure level, we may write the time derivative of α_p as

$$\left(\frac{\partial \alpha_p}{\partial \tau}\right)_p = \left(\frac{\partial \alpha_p}{\partial s^*}\right)_p \frac{\partial s^*}{\partial \tau}. \qquad \text{(A7)}$$

We now use one of Maxwell's fundamental relations that derive from the first law of thermodynamics:

$$\left(\frac{\partial \alpha}{\partial s^*}\right)_p = \left(\frac{\partial T}{\partial p}\right)_{s^*},$$

so that (A6) and (A7) may be written

$$\frac{\partial}{\partial \tau}\text{SPA} = \int_{\text{LFC}}^{\text{LNB}} \Big|_M -\left[\left(\frac{\partial T}{\partial p}\right)_{s^*}\frac{\partial s^*}{\partial \tau} - \frac{\partial \alpha_a}{\partial \tau}\right]dp$$

$$= (T_{\text{LFC}} - T_{\text{LNB}})\frac{\partial s^*}{\partial \tau} + \int_{\text{LFC}}^{\text{LNB}} \Big|_M \frac{\partial \alpha_a}{\partial \tau} dp, \qquad \text{(A8)}$$

where T_{LNB} and T_{LFC} are the temperature in K at the levels of neutral buoyancy and free convection respectively. Given that the change of the parcel's moist entropy is simply proportional to the total heating, $\dot{H}$, divided by the parcel temperature, (A8) may be written

$$\frac{\partial}{\partial \tau}\text{SPA} = \frac{T_{\text{LFC}} - T_{\text{LNB}}}{T_p}\dot{H} + \int_{\text{LFC}}^{\text{LNB}} \Big|_M \frac{\partial \alpha_a}{\partial \tau} dp. \qquad \text{(A9)}$$

The integrand on the right of (A9) can also be expanded in a similar fashion. For an unsaturated environment, it is convenient to regard α as a function of the dry entropy, s, and p:

$$\left(\frac{\partial \alpha_a}{\partial \tau}\right)_{p,M} = \left(\frac{\partial \alpha_a}{\partial s}\right)_p \left(\frac{\partial s_a}{\partial \tau}\right)_{p,M} = \left(\frac{\partial T}{\partial p}\right)_s \left(\frac{\partial s_a}{\partial \tau}\right)_{p,M}. \qquad \text{(A10)}$$

If it is remembered that the time derivatives above are with respect to a coordinate system moving with the parcel to be lifted, we can write in geostrophic coordinates

$$\left(\frac{\partial s_a}{\partial \tau}\right)_{M,p} = \frac{ds_a}{dt} - (\mathbf{V}_{ga} - \mathbf{V}_{gp})\cdot \nabla_X s_a - \omega_a \left(\frac{\partial s_a}{\partial p}\right)_X,$$

where $\mathbf{V}_{ga}$ and $\mathbf{V}_{gp}$ are the geostrophic velocities of the environment and at the parcel origin level, respectively, and ω_a is the ambient pressure velocity (omega); ∇_X denotes the gradient operator in geostrophic coordinates. Neglecting radiative heating and using the above expansion, (A10) may be written

$$\left(\frac{\partial \alpha_a}{\partial \tau}\right)_{p,M} = -\left(\frac{\partial T}{\partial p}\right)_s \left[(\mathbf{V}_{ga} - \mathbf{V}_{gp})\cdot \nabla_X s_a + \omega_a \left(\frac{\partial s_a}{\partial p}\right)_X\right]$$

(unsaturated environment)

$$= -\alpha_a \left[(\mathbf{V}_{ga} - \mathbf{V}_{gp})\cdot \nabla_X \ln\theta + \omega_a \left(\frac{\partial \ln\theta_a}{\partial p}\right)_X\right]. \qquad \text{(A11a)}$$

When the environment is saturated, α_a can be regarded

as being a function of p and s^* and an expression similar to (A11a) results:

$$\left(\frac{\partial \alpha_a}{\partial \tau}\right)_{p,M} = -\left(\frac{\partial T}{\partial p}\right)_{s^*} \times \left[(\mathbf{V}_{ga} - \mathbf{V}_{gp}) \cdot \nabla_X s_a^* + \omega_a \left(\frac{\partial s_a^*}{\partial p}\right)_X\right]. \quad \text{(A11b)}$$

But since

$$\left(\frac{\partial T}{\partial p}\right)_{s^*} \nabla_{X,p} s_a^* = \left(\frac{\partial T}{\partial p}\right)_s \nabla_{X,p} s_a,$$

Eq. (A11b) may be written

$$\left(\frac{\partial \alpha_a}{\partial \tau}\right)_{p,M} = -\alpha_a (\mathbf{V}_{ga} - \mathbf{V}_{gp}) \cdot \nabla_X \ln\theta_a - \left(\frac{\partial T}{\partial p}\right)_{s^*} \omega_a \left(\frac{\partial s_a^*}{\partial p}\right)_X. \quad \text{(A11c)}$$

(saturated environment)

Using (A11a) and (A11c), (A9) becomes

$$\frac{\partial}{\partial \tau} \text{SPA} = \frac{T_{\text{LFC}} - T_{\text{LNB}}}{T_p} H - \int_{\text{LFC}}^{\text{LNB}} \Big|_M - \int_{\text{LFC}}^{\text{LNB}} \Big|_M \left[(\mathbf{V}_{ga} - \mathbf{V}_{gp}) \cdot \nabla_X \ln\theta_a + q_p \omega_a\right] \alpha_a dp, \quad \text{(A12)}$$

where

$$q_p \equiv \begin{cases} \left(\dfrac{\partial \ln\theta_a}{\partial p}\right)_X, & \text{unsaturated environment} \\ \dfrac{1}{\alpha_a}\left(\dfrac{\partial T}{\partial p}\right)_{s^*}\left(\dfrac{\partial s_a^*}{\partial p}\right)_X, & \text{saturated environment.} \end{cases}$$

To the extent that variations with pressure can be accounted for by variations in height alone, we use the hydrostatic relation to write (A12) in the approximate form

$$\frac{\partial}{\partial \tau} \text{SPA} \approx \frac{T_{\text{LFC}} - T_{\text{LNB}}}{T_p} \dot{H} + \int_{\text{LFC}}^{\text{LNB}} \Big|_M g(\mathbf{V}_{ga} - \mathbf{V}_{gp}) \cdot \nabla_X \ln\theta_a + W_a q_a dZ,$$

where W_a is the ambient vertical velocity, and

$$q_a \equiv \begin{cases} g \dfrac{\partial \ln\theta_a}{\partial Z}, & \text{unsaturated environment} \\ g \dfrac{\Gamma_m}{\Gamma_d} \dfrac{\partial \ln\theta_{ea}}{\partial Z}, & \text{saturated environment.} \end{cases}$$

This completes the derivation of (19).

REFERENCES

Austin, P. M., 1960: Microstructure as described by quantitative radar data. *Geophys. Monogr.*, **5**, 85–92.

Bennetts, D. A., and B. J. Hoskins, 1979: Conditional symmetric instability—a possible explanation for frontal rainbands. *Quart. J. Roy. Meteor. Soc.*, **105**, 945–962.

Carbone, R. E., 1982: A severe frontal rainband. Part I: Storm wide hydrodynamic structure. *J. Atmos. Sci.*, **39**, 258–279.

Elliot, R. D., and E. L. Hovind, 1964: On convection within Pacific Coast storms and their relation to structure. *J. Appl. Meteor.*, **3**, 143–154.

Emanuel, K. A., 1979: Inertial instability and mesoscale convective systems. Part I: Linear theory of inertial instability in rotating viscous fluids. *J. Atmos. Sci.*, **36**, 2425–2449.

——, 1983a: On assessing local conditional symmetric instability from atmospheric soundings. *Mon. Wea. Rev.*, **111**, 2016–2033.

——, 1983b: The Lagrangian parcel dynamics of moist symmetric instability. *J. Atmos. Sci.*, **40**, 2368–2376.

——, 1985: Frontal circulations in the presence of small moist symmetric stability. *J. Atmos. Sci.*, **42**, 1062–1071.

Harrold, T. W., 1973: Mechanisms influencing the distribution of precipitation within baroclinic disturbances. *Quart. J. Roy. Meteor. Soc.*, **99**, 232–251.

Hobbs, P. V., 1978: Organization and structure of clouds and precipitation on the mesoscale and microscale in cyclonic storms. *Rev. Geophys. Space Phys.*, **16**, 741–755.

Hoskins, B. J., 1975: The geostrophic momentum approximation and the semi-geostrophic equations. *J. Atmos. Sci.*, **32**, 233–242.

——, I. Draghici and H. C. Davies, 1978: A new look at the ω equation. *Quart. J. Roy. Meteor. Soc.*, **104**, 31–38.

Houze, R. A., P. V. Hobbs, K. R. Biwas and W. M. Davis, 1976: Mesoscale rainbands in extratropical cyclones. *Mon. Wea. Rev.*, **104**, 868–878.

Lindzen, R. S., and K. K. Tung, 1976: Banded convective activity and ducted gravity waves. *Mon. Wea. Rev.*, **104**, 1602–1617.

Sanders, F., and L. F. Bosart, 1985: Mesoscale structure in the megalopolitan snowstorm of 11–12 February 1983. *J. Atmos. Sci.*, **42**, 1050–1061.